aerospace

MDPI

Article

Study on the Mechanism of Cumulative Deformation and Method for Suppression in Aircraft Panel Riveting

Yonggang Kang [1,*], Siren Song [1], Tianyu Wang [1], Guomao Li [1], Zihao Wang [1] and Yonggang Chen [1,2]

[1] School of Mechanical Engineering, Northwestern Polytechnical University, Xi'an 710072, China; songsiren@mail.nwpu.edu.cn (S.S.); wangtianyu1653@mail.nwpu.edu.cn (T.W.); guomaoli7@163.com (G.L.); wangzhpp3@mail.nwpu.edu.cn (Z.W.); scsrr11@163.com (Y.C.)

[2] Xi'an Aircraft Industry Group Company, Ltd., Xi'an 710089, China

* Correspondence: kangyonggang@nwpu.edu.cn

Abstract: In aircraft panel assembly, the interference fit unevenly distributed along the axial direction of the rivet holes leads to an uneven stress–strain field around the rivet holes. The uneven stress–strain fields of single rivets, when accumulated through multiple rivets, result in overall bending and twisting deformation, severely impacting the assembly coordination quality of the panel. This study introduces a numerical model using a single row of multiple rivets to explore cumulative deformation during both sequential and changing order riveting. The results show that the deformation in sequential riveting is mainly bending-oriented towards the driven head side, with the maximum displacement exhibiting a fluctuating accumulation trend as the number of rivets increase. In contrast, a changing riveting order can lead to a reduction in deformation accumulation. To reveal the technological mechanism behind deformation accumulation during the riveting process, a model correlating to the residual stress field was established. It was indicated that the continuous increase in the maximum equivalent bending moment in the axial section is the primary factor leading to deformation accumulation. Based on this finding, a pre-bending suppression method aimed at reducing the local maximum equivalent bending moment was proposed. Numerical calculations and experimental results showed that the maximum displacement of the specimen was reduced by 73.27%, proving that this method can effectively suppress the cumulative increase in deformation.

Keywords: aircraft panel; multi-rivet joint; deformation accumulation; deformation control; pre-bending

check for updates

Citation: Kang, Y.; Song, S.; Wang, T.; Li, G.; Wang, Z.; Chen, Y. Study on the Mechanism of Cumulative Deformation and Method for Suppression in Aircraft Panel Riveting. *Aerospace* **2024**, *11*, 678. https://doi.org/10.3390/aerospace11080678

Academic Editor: Bosko Rasuo

Received: 1 May 2024
Revised: 13 August 2024
Accepted: 15 August 2024
Published: 16 August 2024

Copyright: © 2024 by the authors. Licensee MDPI, Basel, Switzerland. This article is an open access article distributed under the terms and conditions of the Creative Commons Attribution (CC BY) license (https://creativecommons.org/licenses/by/4.0/).

1. Introduction

The aircraft panel is a critical aerodynamic component, typically constructed from beams, frames, angle pieces, and skins through automated riveting. The formation of rivets results in an unevenly distributed interference fit along the axis of the rivet holes, causing a non-uniformly distributed stress and strain field around the rivet holes [1–3]. As the number of rivets increases, the cumulative effect can cause overall bending and twisting deformations of the panel, severely affecting the assembly accuracy of aircraft structural components and the fatigue life of the riveted joints [4–7].

Researchers have conducted extensive studies on predicting aircraft panel deformation. However, these studies often focus only on the final condition of riveting and tend to overlook deformation in riveting process. In modeling the assembly connection process and predicting deformation, Liang et al. [8] focused on a single lap joint, used the micromechanics approach to create a physical model of the stress around the hole, and developed a three-dimensional finite element model of the riveted joint to simulate the riveting process and the loading conditions. Nejad et al. [9] established a load-displacement calculation model based on the three-dimensional elastoplastic finite element method, which allows for an explicit dynamic analysis of the riveting process. Zhang et al. [10], focusing on unidirectional stress, developed a computational model for various stages of rivet deformation,

and derived formulas for the dimensions of the driven head. Chang et al. [11] proposed a solid-shell model, which significantly improved the computational efficiency of wall panel riveting deformation. Liu et al. [12] equated the deformation effect of a single rivet riveting process on connectors to a bending moment and, through simulation calculations and experimental validation, developed a method aimed at predicting global deformation in fuselage wall panels. Wang [13], integrating finite element calculation results from single rivet riveting, used the thick-walled cylinder theory to analytically model the force of the rivet shank on the hole wall, treating it as a local equivalent pressure and applying it to the overall vertical tail model for predicting riveting deformation. Kondo et al. [14] established a simplified finite element simulation model aimed at the batch riveting process of aircraft wall panels, enabling the prediction of multi-rivet riveting deformation. Ni et al. [15] focused on the riveting process of antenna wall panels and extracted deformation data from local riveting deformation for application in the overall model, reducing the global size error associated with assemblies containing thousands of rivets. Siahaan [16] studied the deformation characteristics of multi-rivet riveting, exploring the effects of riveting spacing, panel thickness, and riveting sequence on post-riveting warping deformation. These studies effectively calculate the riveting deformation of wall panels but focus solely on the final state after all rivets have been riveted, with less consideration given to the deformation patterns and process mechanisms during the intermediate riveting stages. In terms of deformation control, Yin et al. [17] explored the pattern of influence of single-rivet, single-factor riveting process parameters on the thickness-direction deformation of thin-walled parts, using rivet spacing and riveting sequence as variables to establish numerical models for deformation control in double-rivet, triple-rivet, quadruple-rivet, and ten-rivet structures. Wang et al. [18] proposed a single-rivet riveting process parameter optimization method based on the Kriging–particle swarm approach for wall panel riveting structures, effectively reducing uneven deformation after riveting through the optimal selection of riveting sequence, riveting force, and other parameters. Yang [19] established a local equivalent thermal expansion model based on the residual stress field and displacement field around the rivet hole, which is used to optimize parameter control for multi-rivet wall panel riveting deformation. Xu et al. [20] employed the Taguchi method, grey relational analysis, and weighting methods to determine the optimal riveting process parameters. Han et al. [21] integrated multiple assembly constraints and rules into the assembly model to ensure a logical sequence and combined symbiotic organism search with ant colony optimization to compute the optimal or near-optimal assembly sequence. Chen et al. [22] employed the extended Stroh formalism and perturbation techniques to derive explicit expressions for the field intensity factors and the image forces on the dislocation as functions of the dislocation's position and material constants.

Despite numerous studies, research on bending and twisting deformations caused by multiple rivet connections remains limited, particularly in terms of the cumulative deformation patterns during the step-by-step riveting process. With the increasing demands for stability and quality in aircraft models, understanding the mechanical process mechanisms behind wall panel deformation accumulation and proposing effective deformation control techniques has become increasingly urgent.

This paper addresses the existing gap in the literature, which typically focuses on the final riveting condition while ignoring the deformation in riveting processes. Firstly, we establish a finite element relay calculation model to predict deformation from multiple-rivet connections. Secondly, this study explores the cumulative patterns of deformation in multi-rivet connections, analyzing the rules of deformation during sequential riveting and investigating how deformation can be reduced in varied sequencing of riveting processes. Thirdly, a model that links residual stress fields with riveting deformation is established to elucidate the mechanical mechanisms behind cumulative deformation during riveting. Finally, we propose a pre-bending riveting technique designed to reduce local maximum equivalent bending moments, whose effectiveness is validated through numerical calculations and experimental testing.

2. Finite Element Modeling

Figure 1a shows the layout and dimensions of Specimen 1, which contains 10 rivets. The total length of the specimen is 220 mm, with each rivet spaced 20 mm apart. The height and width of the specimen are 22.5 mm and 4.5 mm, respectively. Figure 1b shows the layout and dimensions of Specimen 2, which contains 20 rivets. The total length of the specimen is 420 mm, maintaining the same height and width as Specimen 1. Figure 1c also shows the dimensions of a single rivet, with a diameter of 12 mm and a length of 7.2 mm. Figure 1d presents a detailed diagram of a close-up view of the riveting process. The upper and lower sheets are held by blank holders, and the bucking bar supports the sheets from the opposite side of the riveting direction, the relevant material properties are presented in Table 1. Constraints are applied to all degrees of freedom except the Z-axis to accurately simulate the riveting process.

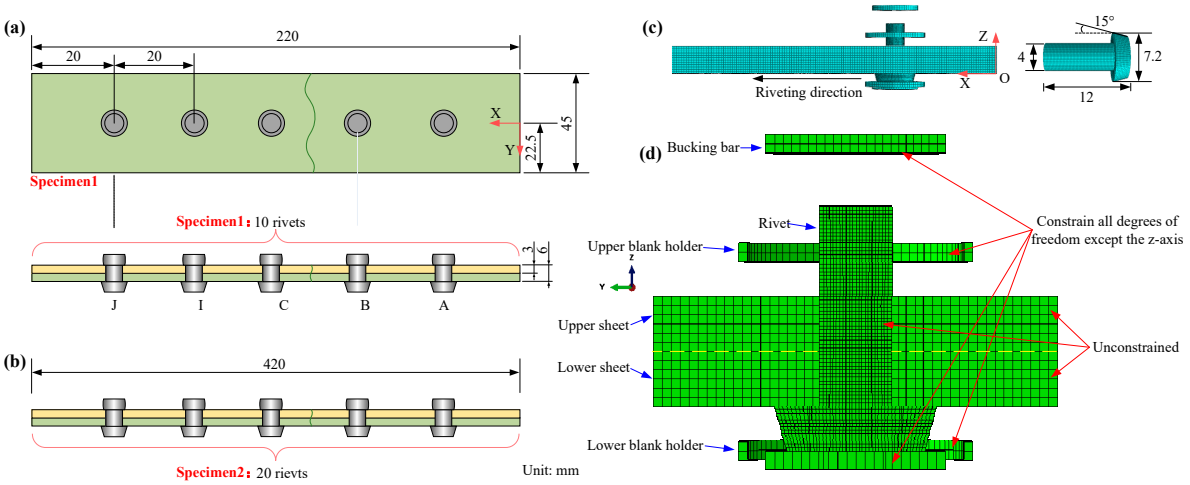

Figure 1. The workpieces and the FEM for the riveting process. (**a**) specimen with ten rivets (**b**) specimen with twenty (**c**) FEM model (**d**) The setup of boundary conditions.

Table 1. Key parameters of the multi-rivet model.

Parameter	Numeric Value/mm	Parameter	Numeric Value/mm
Length of specimen	220/420	The width of the specimen	45
The specimen thickness	6	Nail hole diameter	4.08
Rivet diameter	10	Rivet thickness	1
Friction coefficient μ	0.18	Strength coefficient K of rivet material 2A10	555.61
Press the outer diameter of the rim	13	Hardening exponent n of rivet material 2A10	0.14383
The elastic modulus	71 Gpa	Yield strength σ_s of rivet material 2A10	243 Mpa
Rivet material	2A10	Joining sheet material	Al2024-T3

The rivet is made from 2A10 aluminum alloy, while the specimen utilizes Al 2024-T3 aluminum alloy. The Johnson–Cook model is adopted, with the parameters determined according to the document in [23]. The mesh employs C3D8R cells and utilizes the neutral axis algorithm, accounting for the cylindrical structure, to ensure mesh quality and uniformity along the rivet hole.

The contact algorithm adopts the penalty and dynamic algorithm (represented by P and K, respectively), with the former for the case of a rigid body and the latter for the case without a rigid body. The single-rivet model contains seven instances and seven contact pairs, and the allocation and setting of the contact pairs are shown in Table 2.

Table 2. Master–slave surfaces of a contact pair.

Number	Master Surfaces	Slave Surfaces	Contact Algorithm
1	The lower surface of the burking bar	Rivet stem surface	K
2	The upper surface of the punch	Manufacturing head surface	K
3	The upper surface of the lower blank holder	Lower surface of the lower sheet	p
4	The lower surface of the upper blank holder	Upper surface of thet upper sheet	P
5	The upper surface of the lower sheet	Lower surface of the upper sheet	P
6	The lower surface of the lower sheet and outer surface of the hole	Rivet outer surface	P
7	The upper surface of the upper sheet and outer surface of the hole	Rivet outer surface	P

The calculation and analysis of a single rivet includes three steps: step 1 (pressing process), step 2 (formation process), and step 3 (unloading process). Utilizing the relay calculation model proposed in reference [11], the riveting process of a single rivet is treated as the computational unit and the stress and deformation data generated upon the completion of each rivet's calculations are used as predefined fields for the next calculation [24,25], continuing this sequence until the simulation calculations for all rivets are completed.

3. Cumulative Accumulation of Multiple Rivets

This section examines the residual stress and deformation displacement field of the specimen after the completion of the riveting process, exploring the effects of different riveting sequences on the cumulative deformation of the specimen. Subsequently, case studies of sequential and changing order riveting are selected for an in-depth comparative analysis. It is assumed that the cross-section of the beam remains planar and perpendicular to the beam's axis both before and after deformation. According to the theory of simple bending, it is assumed that after deformation, there is no normal stress between the longitudinal fibers of the beam.

3.1. Investigation of the Cumulative Deformation Rules of Specimen 1 during Sequential Riveting

3.1.1. Radial Residual Stress Distribution

Figure 2 provides a detailed visualization of the radial residual stress distribution in the specimen at various distances from the rivet hole axis. The residual stresses were measured at different points along the Z-coordinate to understand the stress distribution through the thickness of the specimen. After the completion of riveting with a single rivet, a radially distributed residual stress field is formed around the rivet hole, characterized by an axial non-uniform distribution. The selected measurement positions were located at radial distances Δr = 4 mm, 5 mm, 6 mm, 6.7 mm, and 7.5 mm from the rivet hole axis. The results indicate that the residual stresses are predominantly compressive and exhibit a non-uniform distribution trend of decreasing magnitude from top to bottom, with the maximum stress value reaching 283.05 MPa. As the radial distance from the rivet increases, the internal residual stresses of the specimen gradually decrease, with the maximum compressive stress at Δr = 7.5 mm reducing to 75.4 MPa.

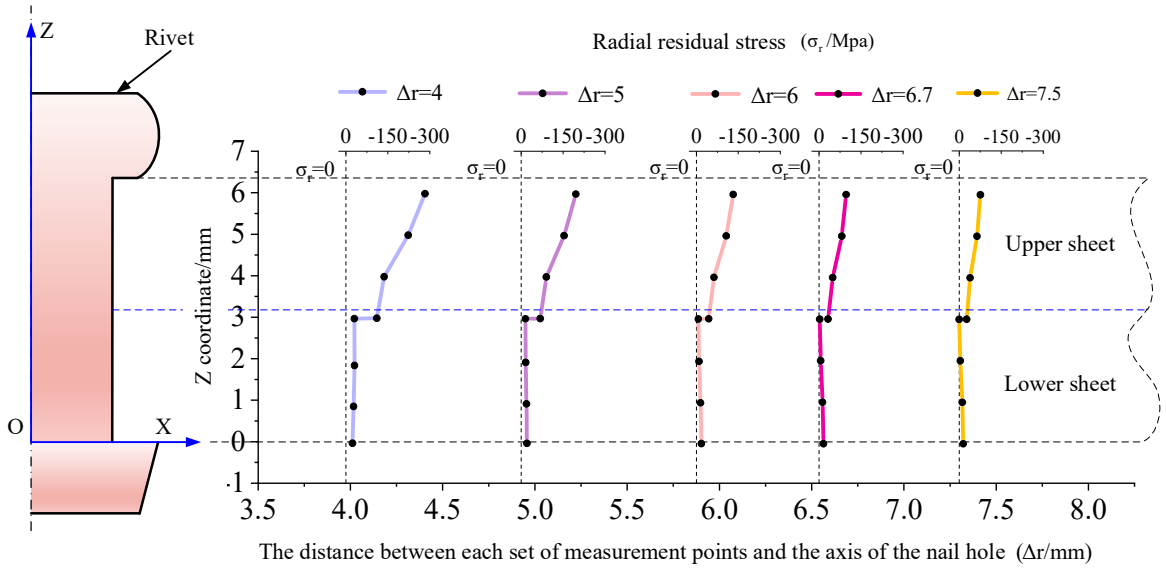

Figure 2. Distribution of radial stress around the hole.

3.1.2. Accumulation of and Change in Deformation

After completing the simulation calculations for all rivets, the Z-direction displacement contour maps were extracted for the specimen following each riveting. Warping and denting deformations of the specimen were observed. The displacement contour maps of the specimen following the riveting of rivets 1 through 10 are depicted in Figure 3.

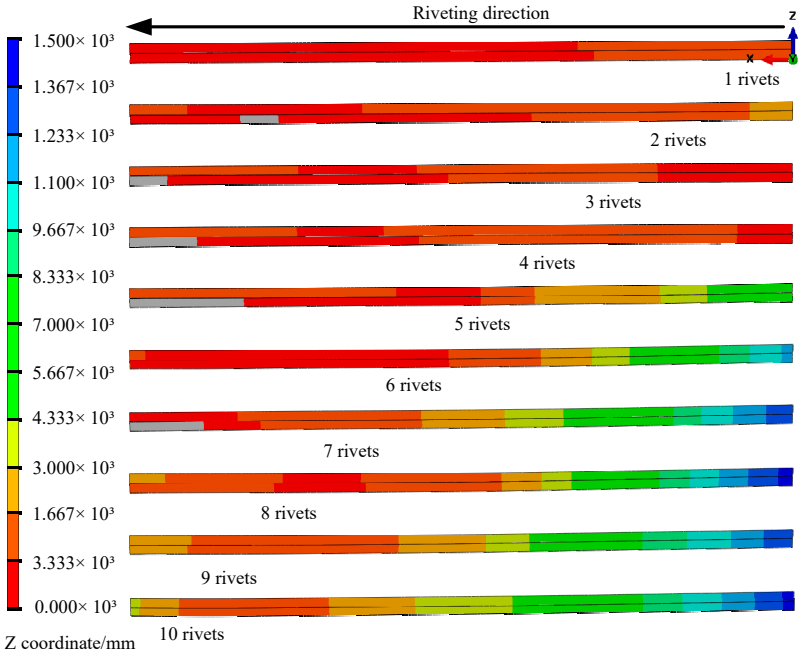

Figure 3. Z-direction displacement after riveting for each rivet (ten rivets).

Figure 4 illustrates the central axial path (Path 1) and the key measurement point A within the 10-rivet specimen, both of which effectively reflect the overall deformation distribution and maximum deformation post-riveting. After each riveting, the X coordinates and Z-direction displacements of the nodes along Path 1 were extracted. These are plotted in Figure 5 using the end position of the riveting sequence as the reference baseline for deformation calculations. All deformation profiles are integrated and displayed in Figure 6.

Additionally, the Z-direction displacements at measurement point A, post-riveting of each rivet, are shown in Figure 7.

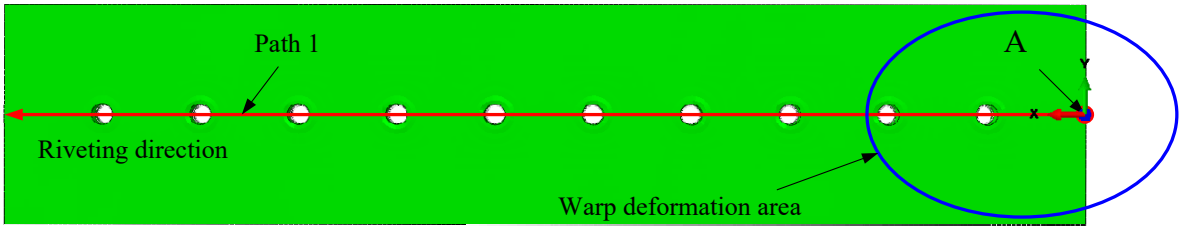

Figure 4. Path 1 and the key measurement point A.

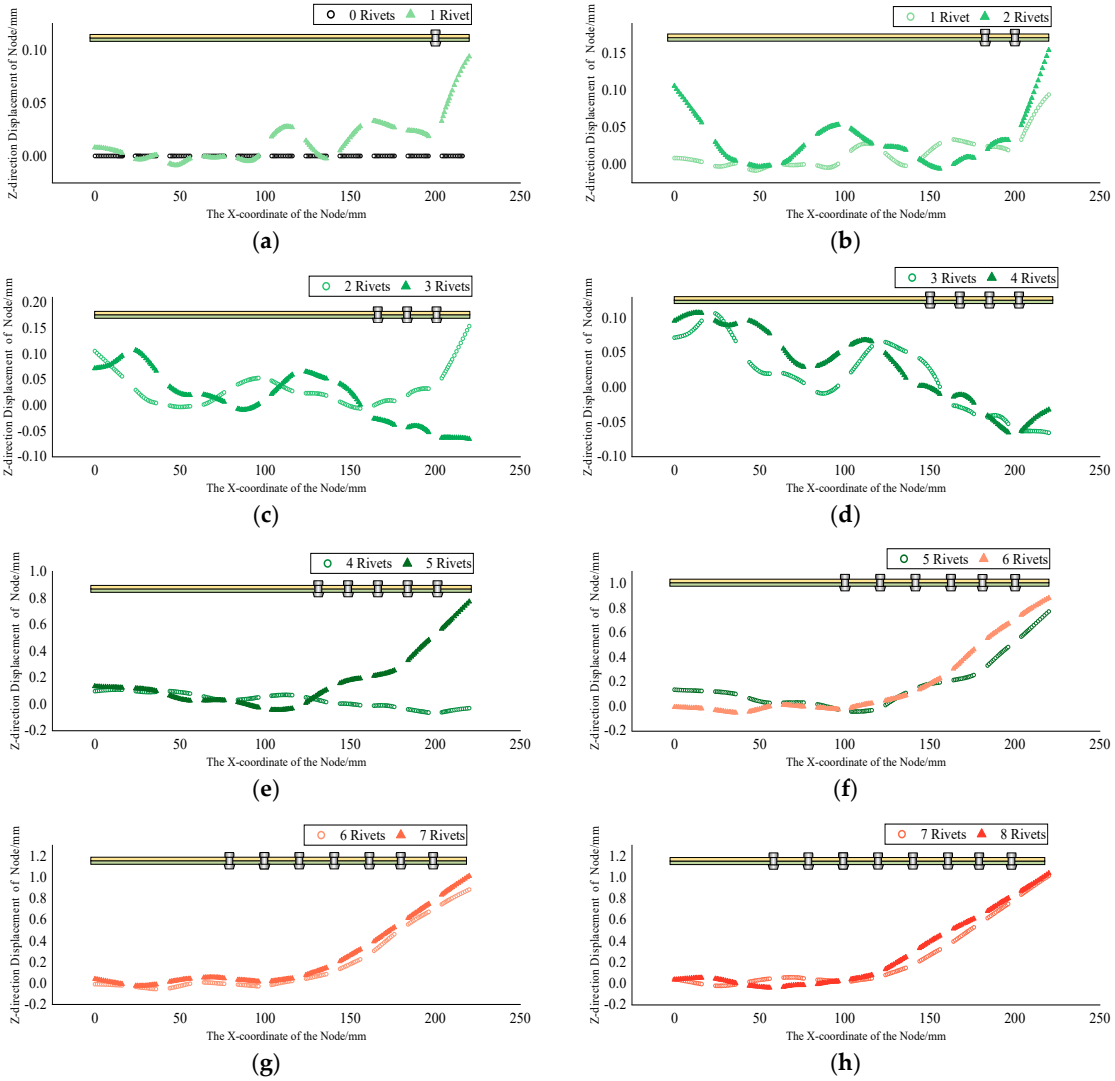

Figure 5. *Cont.*

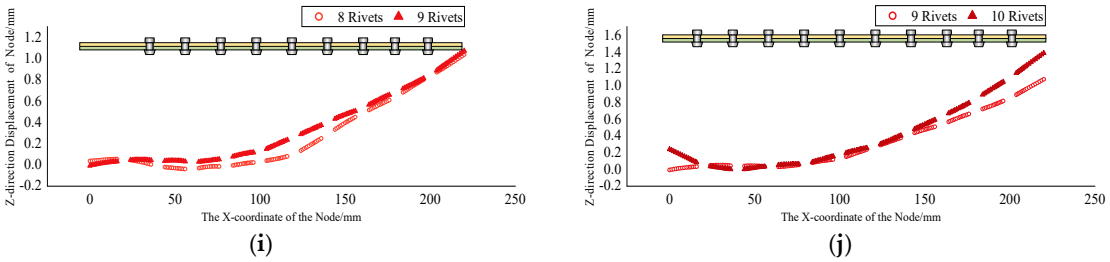

Figure 5. Riveting deformation accumulation. (**a**) Central axis displacement of the specimen before riveting 1 rivet. (**b**) The displacement of the central axis after riveting 1 rivet and 2 rivets. (**c**) Central axis displacement after riveting of rivets and 3 rivets. (**d**) Central axis displacement after riveting 3 rivets and 4 rivets. (**e**) Central axis displacement after riveting 4 rivets and 5 rivets. (**f**) Central axis displacement after riveting 5 rivets and 6 rivets. (**g**) Central axis displacement after riveting 6 rivets and 7 rivets. (**h**) Central axis displacement after riveting 7 rivets and 8 rivets. (**i**) Central axis displacement after riveting 8 rivets and 9 rivets. (**j**) Central axis displacement after riveting 9 rivets and 10 rivets.

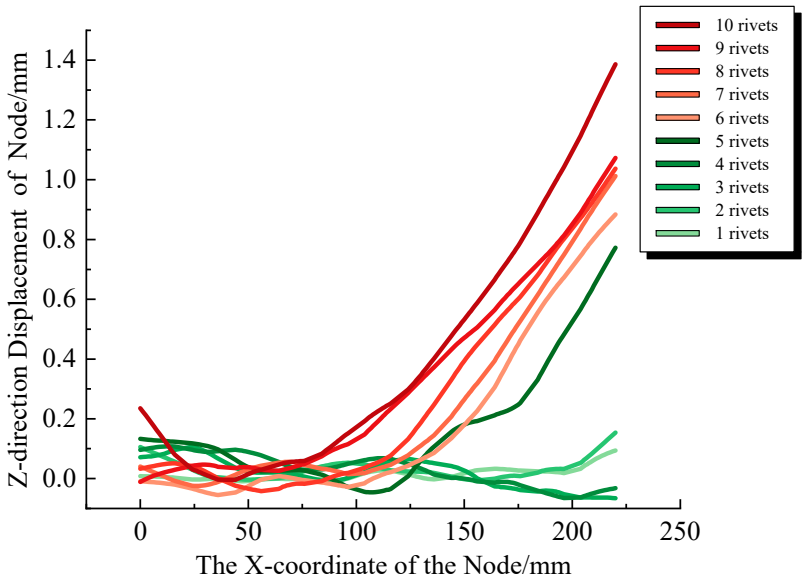

Figure 6. Z displacement of the central axis nodes in sequential riveting of a ten-rivet workpiece.

As depicted in Figure 5a–d, the Z-direction displacements of the specimen after the first four rivets are relatively minor, with no evident regular patterns, and the maximum displacement is approximately 0.1 mm. However, after the fifth rivet, the Z-direction displacement of the specimen significantly increases, with the maximum displacement reaching about 0.8 mm. From this point onwards, the deformation of the specimen exhibits a noticeable regularity, particularly with the progressive accumulation of warping deformation at the right end.

As illustrated in Figures 5e–j, 6 and 7, following the fifth rivet, as riveting progresses, the completed sections of the specimen's central axis begin to display a continuous arched curve, while the sections yet to be riveted maintain a straight-line shape. Upon complete riveting, the central axis assumes a continuous arched form. This indicates that sequential riveting may lead to a continuous accumulation of deformation in the specimen.

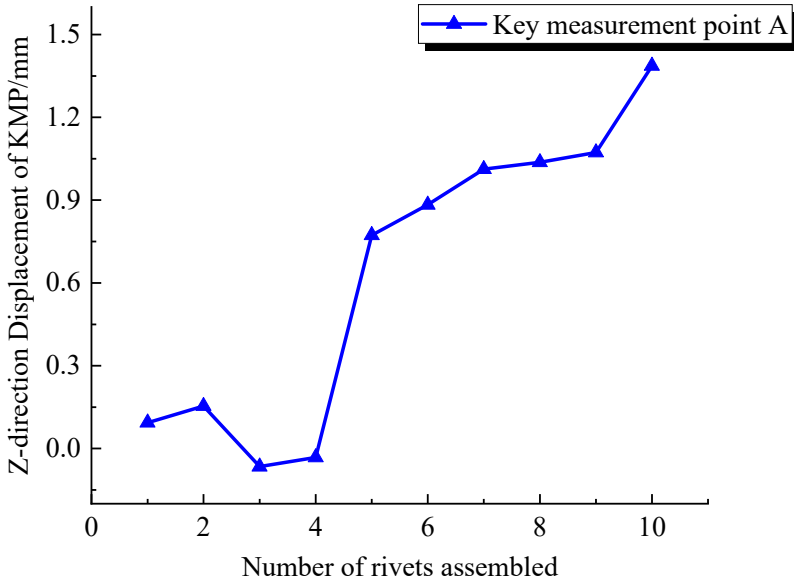

Figure 7. The Z displacement of measuring point A.

3.2. Investigation of the Cumulative Deformation Pattern of Specimen 1 under Changing Order Riveting

According to [13], the riveting sequence alters the constraint conditions of the specimen during the riveting process, thereby affecting the final deformation appearance. Proper planning of the riveting sequence can reduce the deformation of the specimen to some extent. This study continues using Specimen 1 with ten rivets, analyzing the cumulative process of deformation under changing order riveting. Figure 8 shows a schematic of the riveting sequence using the changing order method for ten rivets.

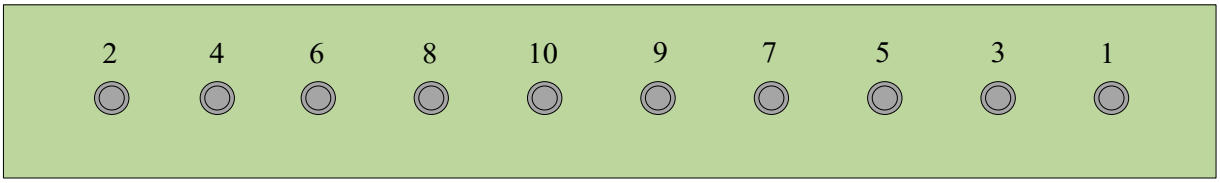

Figure 8. Riveting sequence changing method.

Finite element calculations were performed, and the deformations of the specimen post-riveting of each rivet were extracted, as shown in Figure 9, to observe the cumulative deformation patterns following each rivet connection. Furthermore, for a comparative analysis, all data are consolidated in Figure 10.

Unlike sequential riveting, changing order sequence riveting does not exhibit a continuous accumulation of warping deformation at one end. Instead, the specimen displays various deformation morphologies, including convex and concave shapes. After riveting the 1st, 2nd, 4th, 5th, 8th, 9th, and 10th rivets, the right end of the sheet shows a tendency for upward bending deformation, while the left end exhibits upward bending after the third, sixth, and seventh rivets. Figure 9a,c–e reveal that the initial accumulation areas of bending deformation are at both ends, whereas Figure 9g–j indicate that, after the last four rivets, the accumulation areas gradually shift to the central region of the sheet. This demonstrates that the riveting sequence significantly influences the accumulation of deformation. After the 8th, 9th, and 10th rivets, a notable reduction in deformation occurs, indicating that the changing order method effectively mitigates deformation in the ten-rivet specimen.

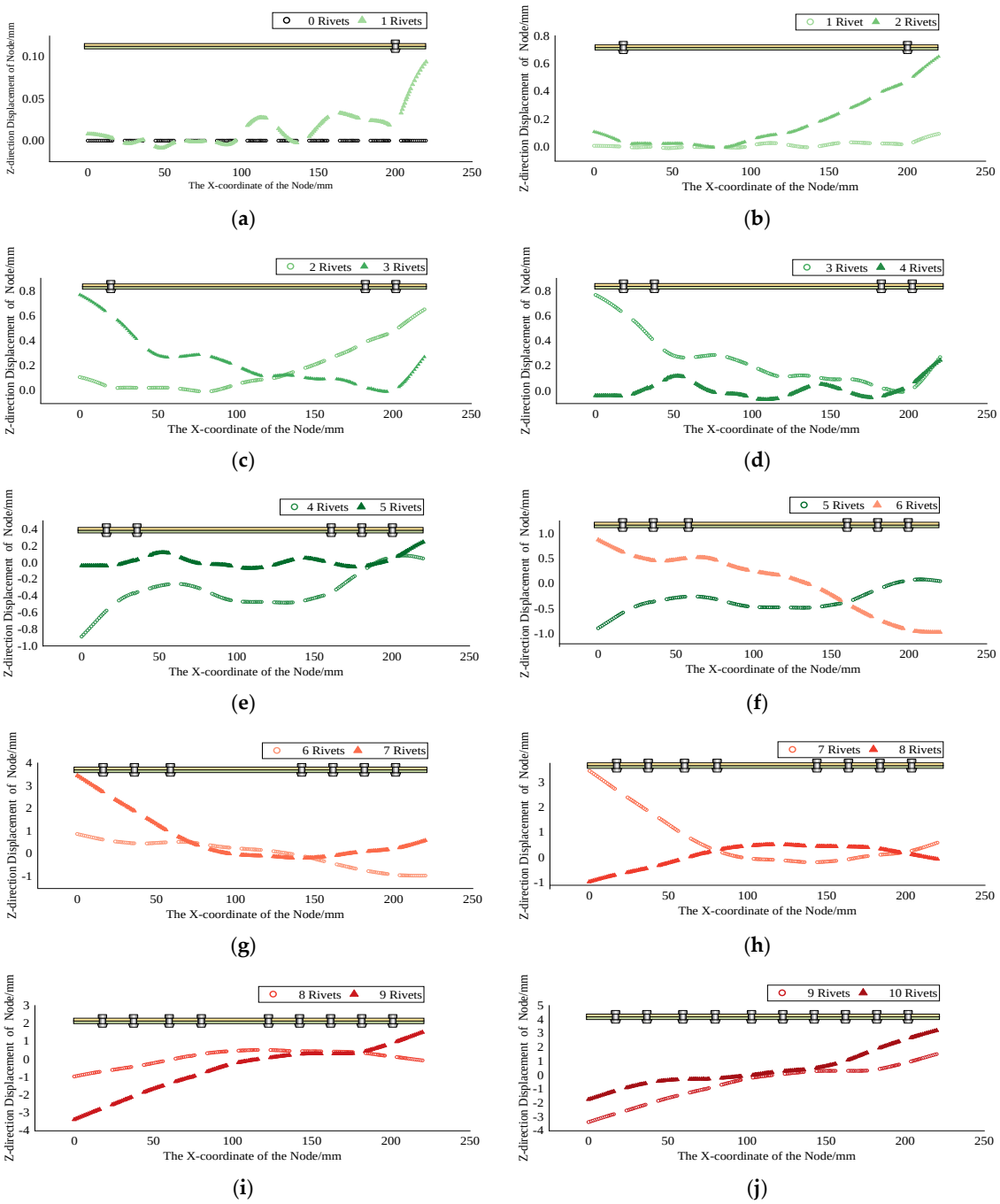

Figure 9. Riveting deformation accumulation. (**a**) Central axis displacement of the specimen before riveting 1 rivet. (**b**) The displacement of the central axis after riveting 1 rivet and 2 rivets. (**c**) Central axis displacement after riveting 2 rivets and 3 rivets. (**d**) Central axis displacement after riveting 3 rivets and 4 rivets. (**e**) Central axis displacement after riveting 4 rivets and 5 rivets. (**f**) Central axis displacement after riveting 5 rivets and 6 rivets. (**g**) Central axis displacement after riveting 6 rivets and 7 rivets. (**h**) Central axis displacement after riveting 7 rivets and 8 rivets. (**i**) Central axis displacement after riveting 8 rivets and 9 rivets. (**j**) Central axis displacement after riveting 9 rivets and 10 rivets.

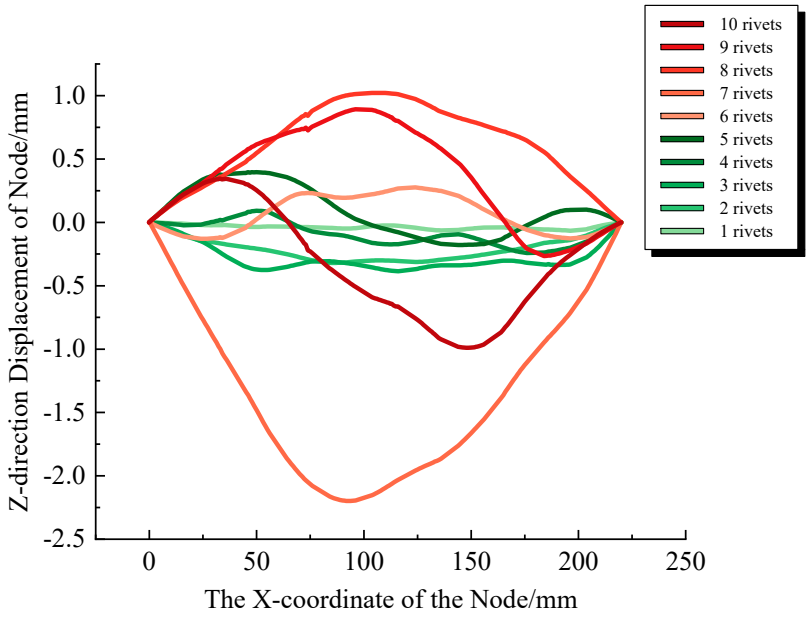

Figure 10. Z-direction displacement of central axis nodes in a ten-rivet specimen with varied sequencing riveting after aligning both ends.

3.3. Deformation Accumulation Rule under Sequential Riveting of Specimen 2

Specimen 2 contains twenty rivets with the cumulative variation in deformation, as shown in Figure 11. The deformation of four rivets was small, but after the fifth rivet, the right end of the larger distortion deformation became displaced; this deformation accumulation effect gradually became more obvious, where after completing 20 rivets, the deformation displacement reached the maximum, at 5.36 mm (riveting started at the end as a benchmark). At present, for the overall bending deformation form, with the increase in the number of riveting, the warping deformation increment gradually becomes more stable and uniform.

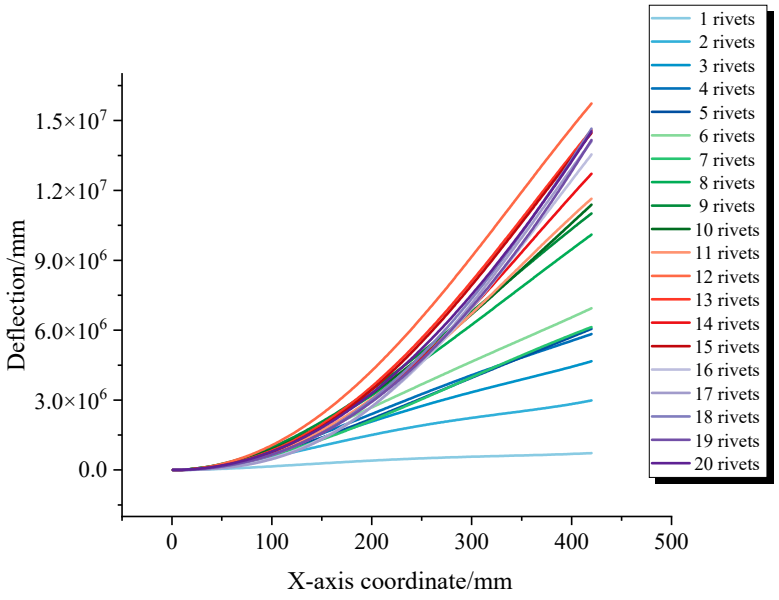

Figure 11. Z-direction displacement of central axis nodes in a twenty-rivet workpiece.

4. The Deformation Active Suppression Method

4.1. Discussion on the Deformation Accumulation Mechanism

To further analyze the correlation between residual stress and deformation displacement, using the finite element analysis results of Specimen 1 as an example, eleven radial stress extraction paths were selected along the longitudinal cross-section at the midpoint between adjacent rivets, spaced 20 mm apart, as shown by the red lines in Figure 12. For Specimen 1, after the completion of ten rivets, the Z coordinates and radial stresses of nodes on these paths were extracted, totaling 110 sets of data, each set containing seven data points. Figure 13 displays the radial residual stress of seven nodes along the second path (hereinafter, referred to as Path2-2-2) after completing two rivets, and the corresponding Z coordinates. To provide a detailed representation of the radial residual stress distribution along the axial direction (Z-direction) of the rivet holes, a linear interpolation method was employed to construct a radial residual stress prediction function, depicted as the blue curve in Figure 13.

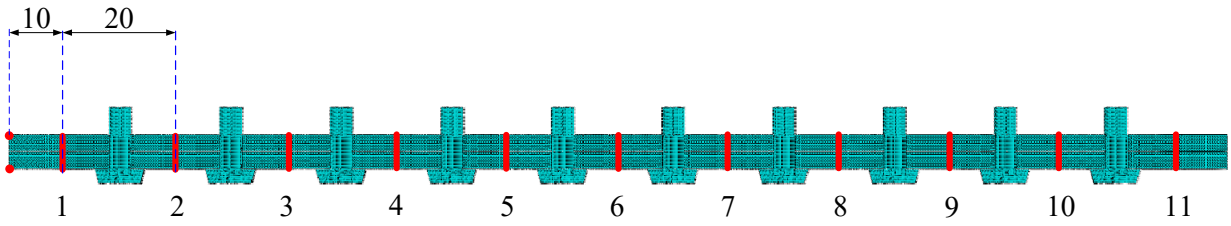

Figure 12. Extraction location for radial residual stress.

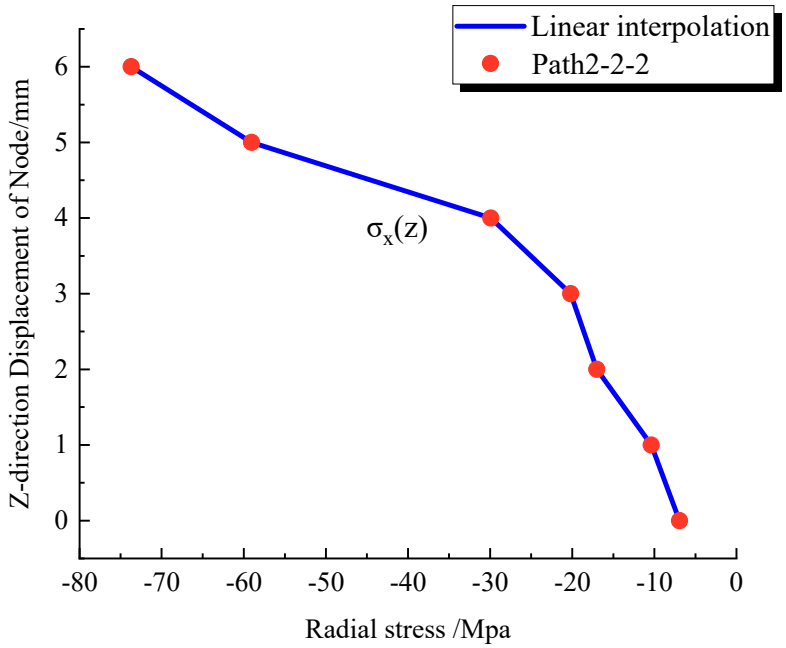

Figure 13. Radial residual stress in path 2-2-2 and linear interpolation function.

Figure 14 displays a Z-Y cross-sectional view of the specimen that includes path 2-2-2, where the thicknesses of the upper and lower sheets are t1 and t2, respectively. Given that the specimen's bending deformation around the Y-axis is substantially greater than around the X-axis, it is assumed that the radial residual stresses are uniformly distributed along the Y-axis within any Z-Y cross-section, as shown by the red lines in Figure 14. Based on this assumption, the bending moment My around the Y-axis of this cross-section

can be calculated using the relevant formulas, where t represents the total thickness of the specimen.

$$M_y = \int_0^{(t_1+t_2)} \sigma_x(z)(z - \frac{t}{2})dz \quad (1)$$

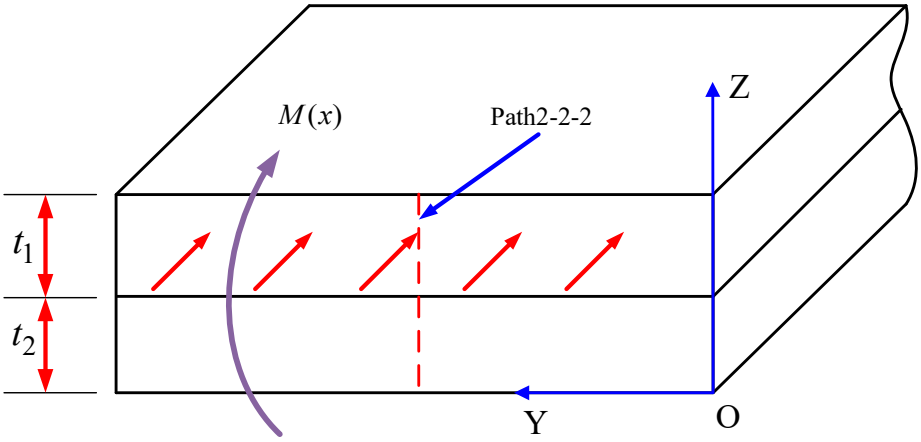

Figure 14. Assumption of uniform distribution of radial residual stress along the Y-direction.

Figure 15 illustrates the bending moment distribution for a ten-rivet specimen after riveting seven rivets, where the red dots represent the bending moments calculated according to Equation (1), totaling eleven points. From Figure 15, it can be observed that the equivalent bending moments are larger in the middle and smaller at the ends, indicating a distribution trend that decreases from the center towards both sides.

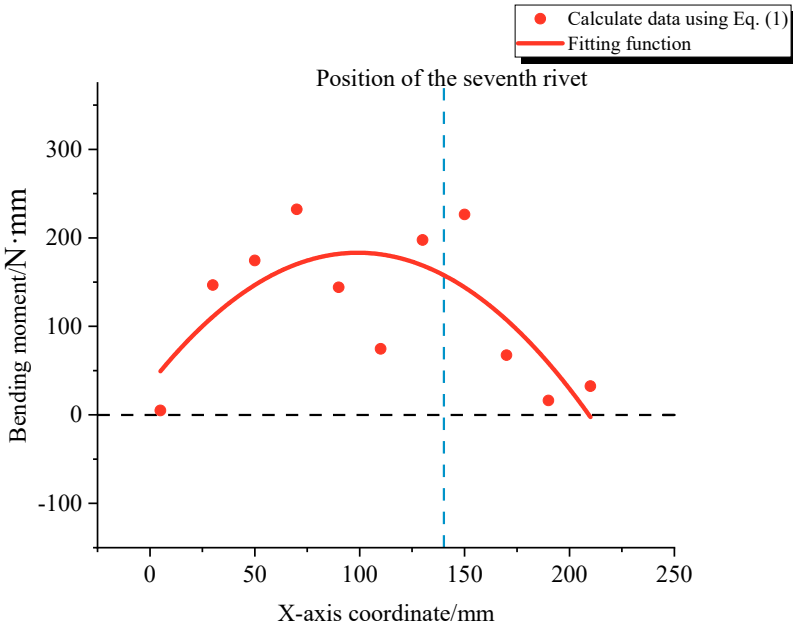

Figure 15. Bending moment distribution after riveting 7 rivets with 10 rivets.

Utilizing a consistent fitting method, the equivalent bending moment distribution for the specimen can be obtained after the riveting process is completed, as shown in Figure 16. It is observed that the riveting process induces a positive bending moment within the specimen's cross-section. As the number of completed rivets increases, the position of the maximum equivalent bending moment progressively shifts to the right.

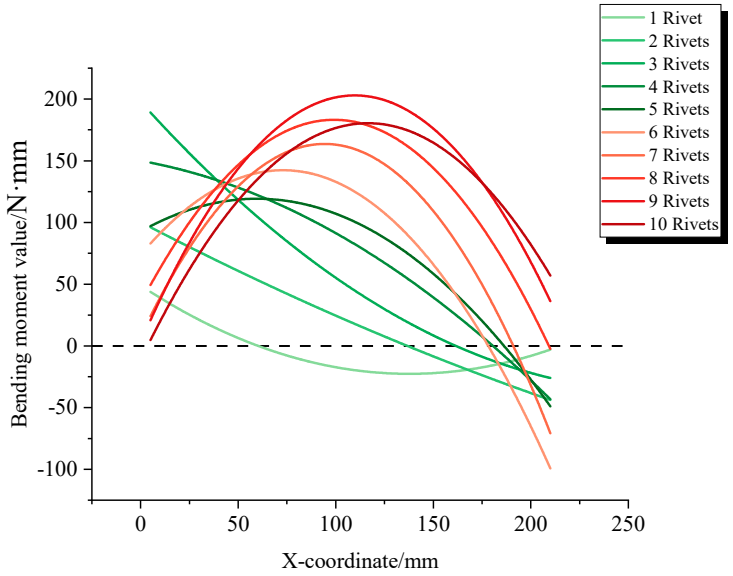

Figure 16. Calculation results of equivalent bending moment.

Based on Euler–Bernoulli beam bending theory, an association model between the equivalent bending moment and deflection of the specimen has been developed, as presented in Equation (2). $P(\mathrm{R,S})$ is a function of factors including the rivet and specimen material properties, as well as geometric dimensions.

$$P(R,S)\frac{d^2w(x)}{dx^2} = M(x) \tag{2}$$

The deflection deformation of the specimen can be obtained through Equation (3):

$$w(x) = P(R,S)\int_m^n \int_m^n M(x)dxdx \tag{3}$$

For the specimen with ten rivets, its length is specified as [m, n] = [0, 220] mm. Assuming $p(R,S) = 1$, by synergistically utilizing Equations (1) and (3), the variation in deflection due to bending deformation of the specimen can be calculated. The outcomes of these calculations are displayed in Figure 17.

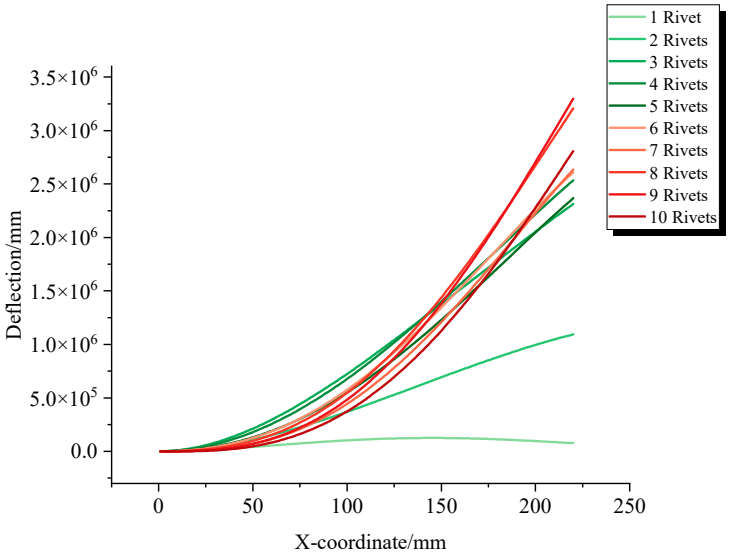

Figure 17. Calculation results of deflection of a 10-rivet workpiece.

The equivalent bending moment–deflection correlation model, which utilizes radial residual stresses extracted from a multi-rivet sequential relay calculation model as input, determines the specimen's deflection deformation, as illustrated in Figure 17. Comparing this with Figure 6, it is evident that the trends of analytical and numerical calculation results are consistent. As the number of completed rivets increases, the bending deformation of the specimen becomes more pronounced, with significant accumulative deformation displacement occurring at one end of the specimen. Therefore, it can be asserted that the equivalent bending moment–deflection correlation model effectively describes the relationship between the radial stress field and deformation of the specimen.

4.2. The Pre-Bending Active Suppression Method

According to Equation (3), an increase in the equivalent bending moment of a specimen correlates with a higher non-uniformity in its internal radial residual stress distribution, thereby leading to more pronounced bending deformations. Maximum equivalent bending moments were extracted after the installation of each rivet for specimens with 10 sequential rivets, 10 rivets using the edge method, and 20 sequential rivets, as depicted in Figure 18. The observations indicate that the maximum equivalent bending moments significantly rise after the installation of the initial rivets. In sequential riveting, the maximum bending moment fluctuates around a high value (200 N·mm), while in changing order method riveting, it continuously decreases towards the last few rivets. Correspondingly, the deformation accumulation increment is relatively small for the initial few rivets in sequential riveting but increases significantly for subsequent rivets (as shown in Figures 6 and 11); conversely, in varied sequence riveting, a reduction in deformation is observed in the last few rivets (as shown in Figure 10).

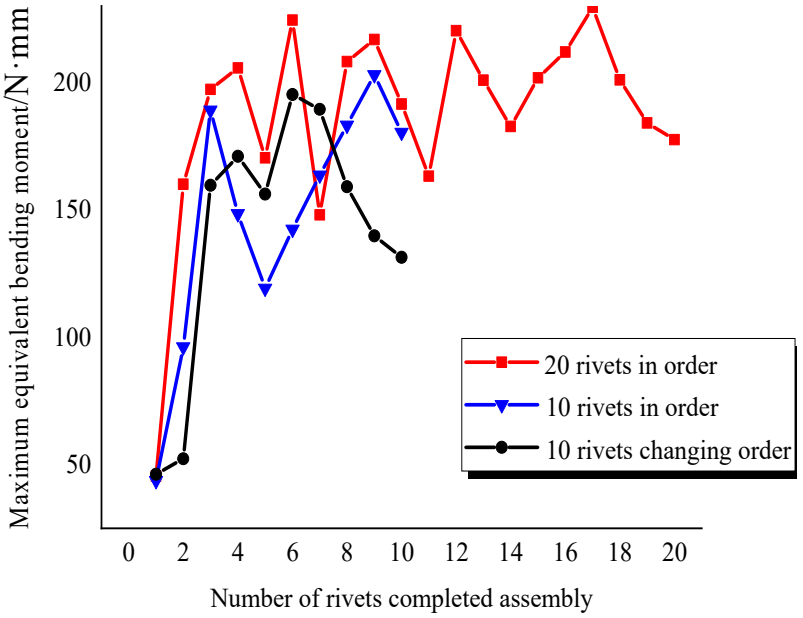

Figure 18. The variation in the maximum equivalent bending moment of the panel with the number of rivets.

Based on the data from Figures 11 and 18, it can be concluded that the smaller the maximum equivalent bending moment of the specimen prior to riveting, the smaller the increment in deformation post-riveting; conversely, the larger the maximum equivalent bending moment, the greater the deformation increment post-riveting. Hence, it can be inferred that reducing the maximum bending moment before riveting can effectively decrease the increment in bending deformation of the specimen after riveting, thereby achieving the goal of controlling riveting deformation and a pre-bending active suppression method for controlling specimen deformation has been proposed: prior to riveting, an

upward forced displacement x_{pre} is applied to the burking bar, inducing a specific elastic bending deformation in the specimen (illustrated with a single rivet installation, as shown in Figure 19). This procedure introduces tensile stress near the driven head side and compressive stress near the manufacturing head side, superimposing these with the existing stress field. As a result, the overall stress field of the specimen is homogenized, reducing the maximum equivalent bending moment. Consequently, this approach effectively lowers the increment in deformation during the riveting process, ultimately achieving the suppression of specimen deformation.

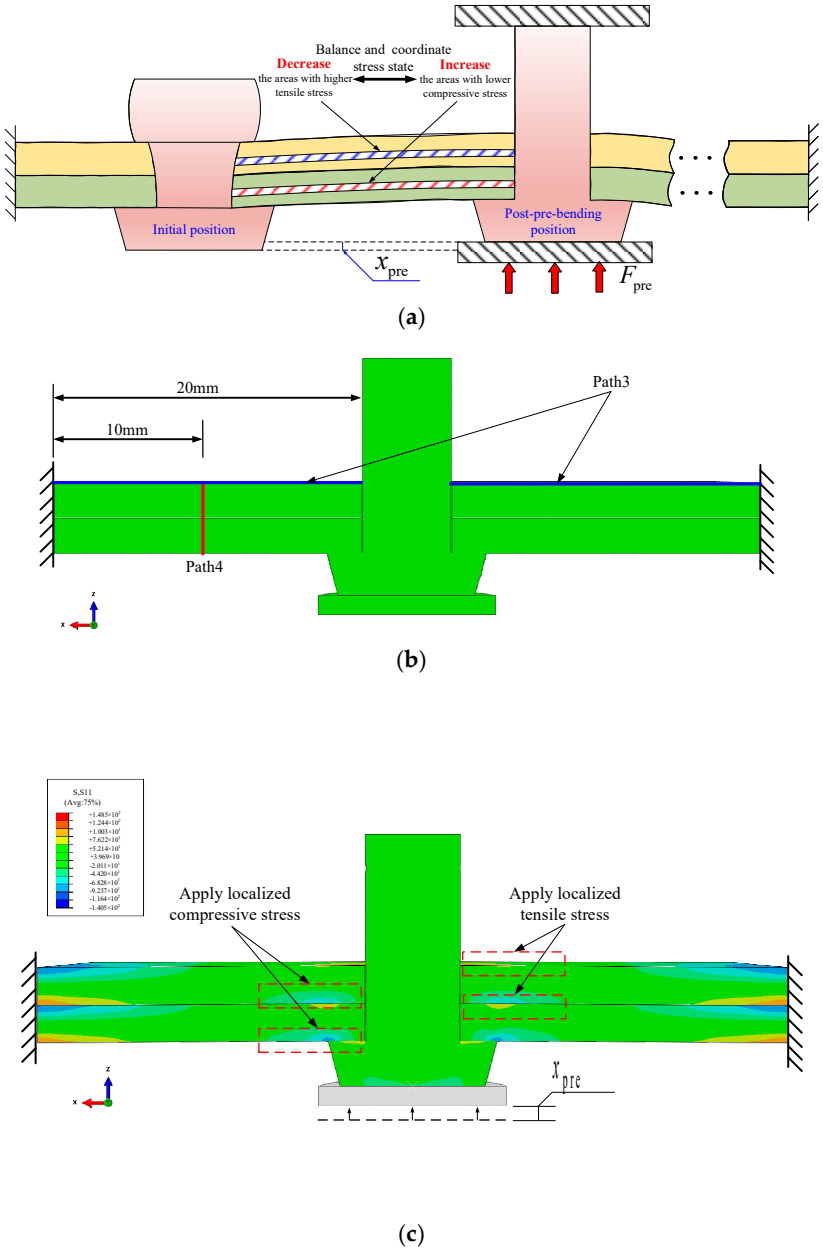

Figure 19. Elastic pre-bending method. (**a**) The pre-bending process method. (**b**) Before applying pre-bending displacement. (**c**) After applying pre-bending displacement.

The upward forced displacement x_{pre} of the rivet is a critical parameter in the pre-bending active suppression method, and its optimization is crucial. To identify the optimal forced displacement parameter, this study utilized a single-rivet joining process as the subject of finite element simulation experiments to evaluate its effectiveness in actively suppressing specimen deformation. Figure 19a illustrates a schematic of the pre-bending

process, while Figure 19b displays the rivet and specimen model before the application of forced displacement x_{pre}, with paths 3 and 4 indicating the displacement extraction and radial stress extraction paths, respectively. Figure 19c shows the distribution of radial stresses in the single-rivet finite element model after the application of forced displacement, revealing that the forced displacement introduces elastic pre-stress near the rivet hole area. Specifically, it induces localized tensile stress near the upper surfaces of the sheets and localized compressive stress near the lower surfaces, which oppose the stress field generated by the riveting process, as depicted in Figure 2.

The forced displacements of the burking bar prior to riveting (pre-applied upward force F_{pre}) were set at 0.1 mm, 0.2 mm, 0.3 mm, 0.32 mm, 0.34 mm, 0.36 mm, 0.38 mm, 0.4 mm, and 0.5 mm, with a finite element model without forced displacement serving as a control group for the numerical simulation calculations. The X and Z coordinates post-riveting were extracted from path 3, as shown in Figure 20. The Z coordinates and radial stresses post-application of pre-stress (before riveting) were extracted from path 4, as displayed in Figure 21. Similarly, the Z coordinates and radial stresses post-riveting were extracted from path 4, as presented in Figure 22.

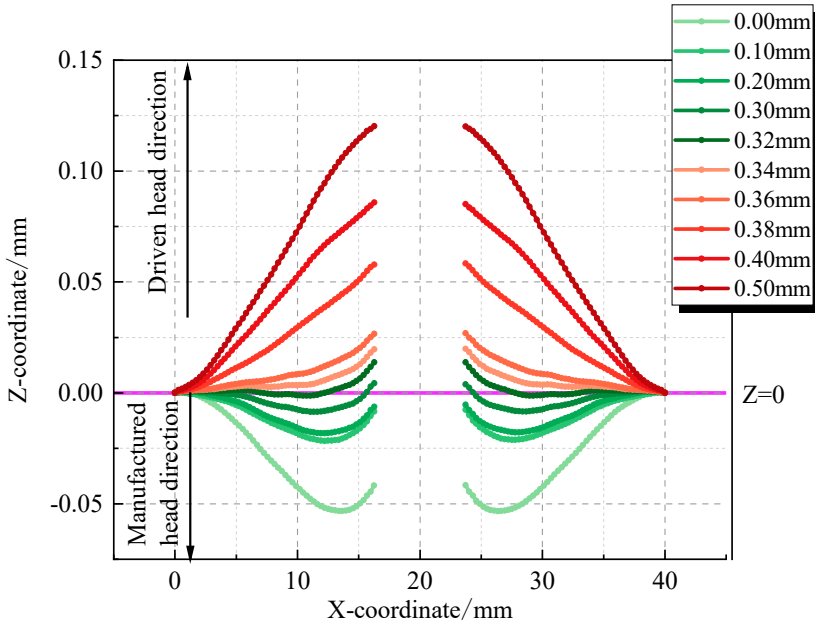

Figure 20. Single-nail pre-bending path 3 node Z-direction displacement.

Figure 20 illustrates that for the Z-direction displacement of nodes within path 3 of the specimen, the control group without forced displacement exhibited a bulging deformation centered around the rivet hole. With increasing forced displacement of the burking bar, the deformation of the specimen progressively decreased. At a forced displacement of x_{pre} = 0.32 mm, the post-riveting deformation of the specimen was more uniform, with the maximum displacement reduced to its smallest value of approximately 0.014 mm, a 72% decrease from the 0.05 mm observed in the no-displacement condition. However, when the forced displacement x_{pre} exceeded 0.32 mm, the specimen began to show inverse indentation deformation, reaching a maximum reverse displacement of 0.12 mm on the upper surface at a displacement of 0.5 mm.

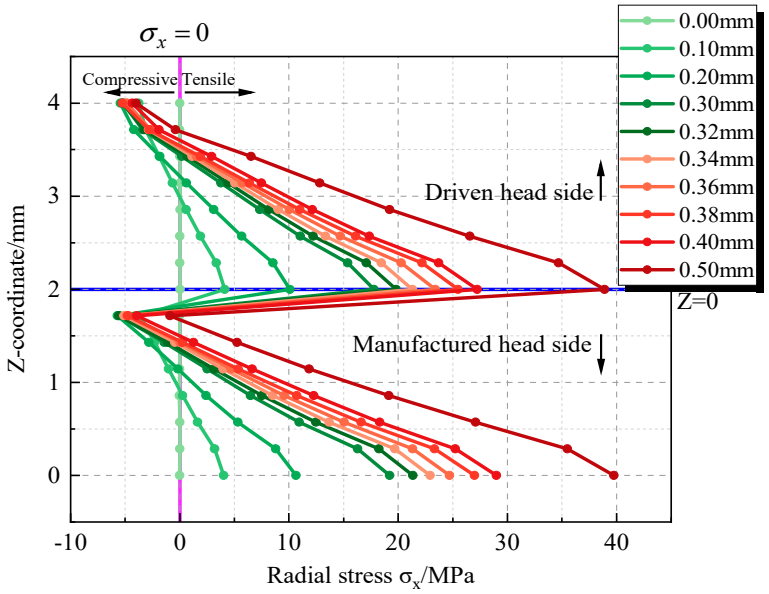

Figure 21. Comparison chart of radial stress data for path 4 after applying pre-stress.

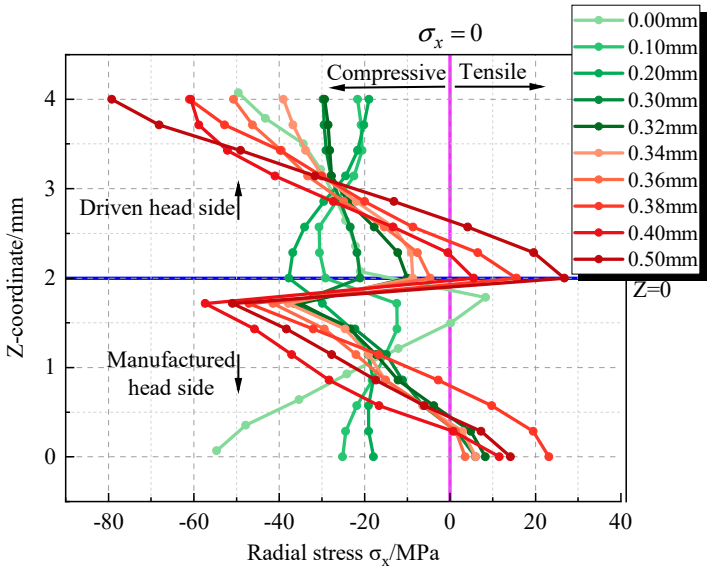

Figure 22. Comparison chart of radial stress data for path 4 after riveting.

Figure 21 demonstrates that for the radial stress distribution of path 4, the control group specimens had 0 radial stress before riveting, aligning with the line $\sigma_x = 0$. As the forced displacement of the burking bar increased, the radial stresses along path 4 increased, displaying a pattern of compressive stress on the upper surfaces and tensile stress on the lower surfaces of both sheets. The maximum radial stress values for each set of experiments typically occurred at the lower surface of the upper sheet or the lower surface of the lower sheet, intersecting with path 4. When the forced displacement load reached 0.5 mm, the radial stress peaked at 39.76 MPa.

Figure 22 illustrates the radial stress distribution in the Z-direction for nodes within path 4 of the specimen. The control group specimens exhibited significant compressive stress distributions on the upper surface of the upper sheet and the lower surface of the lower sheet after riveting, with the maximum compressive stress reaching 54.65 MPa. As the forced displacement load of the burking bar increased, the radial stresses at these locations gradually decreased, leading to a more uniform axial distribution of radial stress. At a forced displacement of x_{pre} = 0.30 mm, the residual stress field in the post-riveted

specimen became more uniform. When the forced displacement reached x_{pre} = 0.32 mm, the uniformity of the residual stress field was optimized, resulting in the most effective suppression of deformation.

4.3. Results Analysis of Pre-Bending Deformation Suppression Experiment

Experiments and validation efforts were carried out for the sequential riveting of 20 rivets. The riveting test environment is shown in Figure 23, where an adapted electronic universal testing machine was used to apply loads to the rivets and a support stand was employed to maintain the specimen in a horizontal position during the riveting process. Figure 24 displays multi-rivet specimens upon completion of riveting.

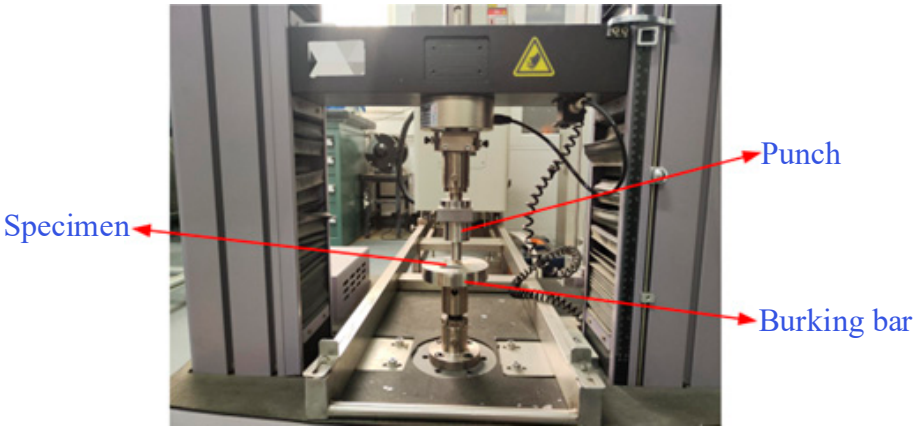

Figure 23. Pressure riveting test environment.

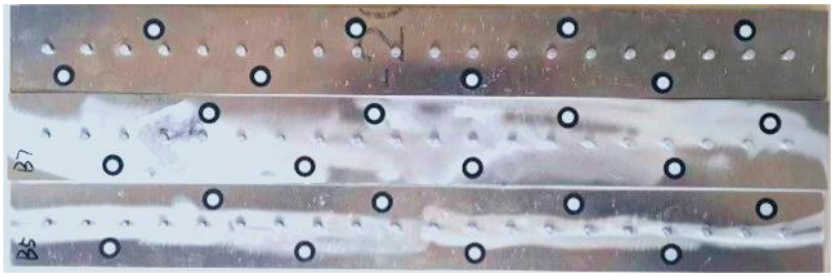

Figure 24. Twenty-rivet workpieces.

Utilizing the Creaform Handyscan 700 scanner, deformation data of the specimen were measured before riveting and after each rivet installation. Figure 25a,b display the displacement along the central axis of the specimen without pre-bending (referred to as the control group); Figure 25c,d show the central axis displacement of the specimen when a forced displacement of 0.32 mm was applied to each rivet (referred to as the deformation suppression group).

Figure 25a,c indicate that specimens from both experimental groups exhibited initial deformation before riveting, with maximum displacements of 5.28 mm and 5.99 mm at zero rivets, showing a minor difference. After riveting 5 and 10 rivets, both groups of specimens exhibited cumulative bending deformations. The control group displayed displacement increments of 0.58 mm and 0.55 mm after riveting 5 and 10 rivets, respectively. In contrast, the deformation suppression group exhibited increments of 0.44 mm and 0.13 mm. Upon comparison, the deformation suppression group showed reductions in maximum displacement increments of 0.14 mm and 0.42 mm after riveting 5 and 10 rivets, respectively.

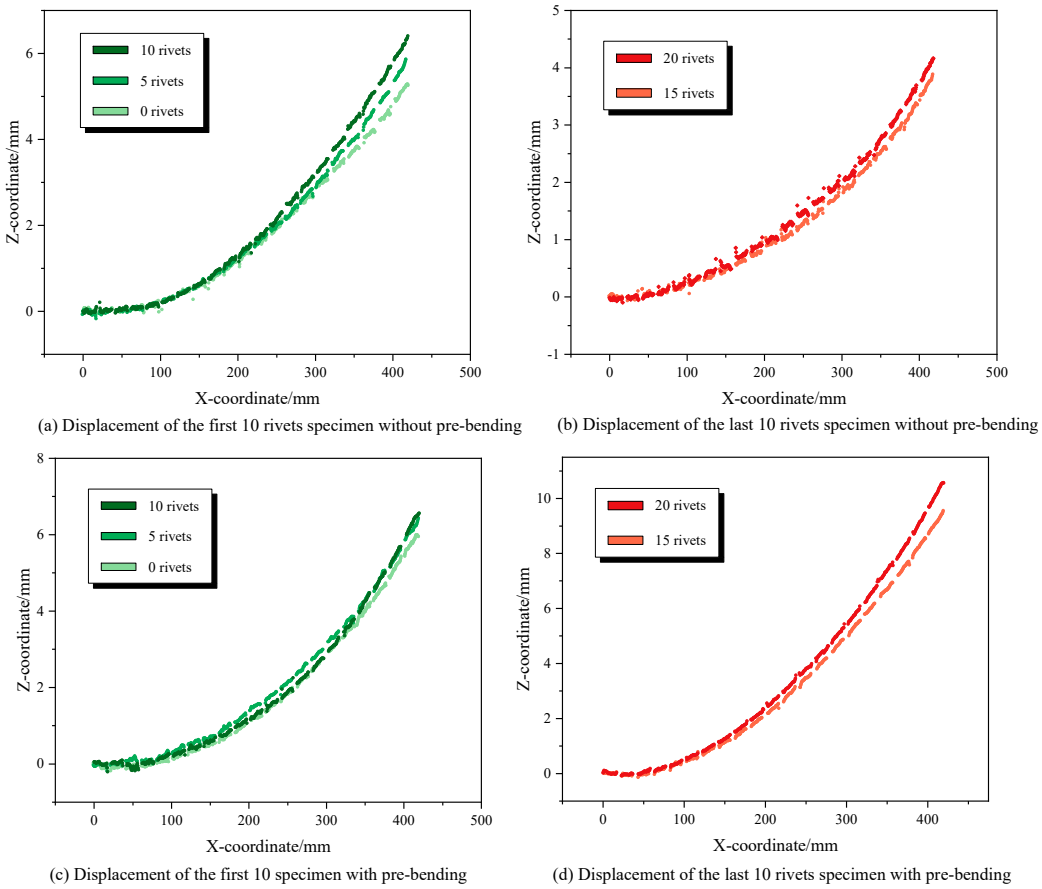

Figure 25. Axis displacement of control group. (**a**) Displacement of the first 10 rivets specimen without pre-bending (**b**) Displacement of the last 10 rivets specimen without pre-bending (**c**) Displacement of the first 10 specimen with pre-bending (**d**) Displacement of the last 10 rivets specimen with pre-bending.

Figure 25b,d illustrate that the control group had maximum displacements of 9.55 mm and 10.56 mm after 15 and 20 rivets, respectively, with an increment of 1.01 mm. In contrast, the deformation suppression group showed maximum displacements of 3.89 mm and 4.16 mm after 15 and 20 rivets, with an increment of 0.27 mm. This indicates a reduction in the maximum displacement increment by 0.74 mm and a 73.27% decrease in the deformation suppression group after 15 and 20 rivets, respectively. Friction between the contacting surfaces of the rivet and the sheets significantly influences the mechanical behavior of the joint. It affects load transfer, stress distribution, and overall joint efficiency. Prediction of deformation and failure modes: Friction impacts the deformation characteristics and potential failure modes of the joint by altering the stress and strain distributions within the materials involved.

5. Conclusions

(1) For multi-rivet specimens, the primary deformation sequence manifests as bending towards the driven head side. As the number of rivets increases, the maximum deformation displacement of the specimen exhibits a fluctuating upward trend, with the cumulative effect of the bending deformation becoming increasingly apparent. Changing order riveting can alter the accumulation location of bending deformation and reduce the maximum deformation trend

(2) Utilizing the Euler–Bernoulli beam bending theory, a correlation model between moment and deflection for the specimen has been developed. This model highlights the

maximum equivalent bending moment at the axial cross-section of the rivet hole prior to riveting as the key factor influencing the progressive accumulation of riveting deformation.

(3) A pre-bending active suppression method has been proposed, which aims to reduce deformation accumulation by minimizing the maximum equivalent bending moment in the local axial section of the rivet hole. Both numerical calculations and experimental results have demonstrated that the pre-bending method significantly reduces the maximum displacement of the specimen, with a reduction of up to 73.27%.

(4) In our current study, we focused on the application of the Euler–Bernoulli beam theory primarily due to its relevance and simplicity for the initial analysis of deformation in riveted joints. This approach allowed us to establish baseline predictions that are both computationally efficient and sufficiently accurate for the scope of this investigation. Additionally, a non-linear analysis could reveal the different stress and deformation behaviors, particularly under high loading conditions where non-linear material properties such as plasticity and large deformations come into play. Future studies should incorporate non-linear analyses to provide a more comprehensive understanding of the mechanical behavior under various riveting conditions.

Author Contributions: Software, S.S., T.W., G.L. and Z.W.; Formal analysis, T.W.; Writing—original draft, S.S.; Writing—review & editing, Y.K.; Supervision, Y.K.; Project administration, Y.C.; Funding acquisition, Y.K. All authors have read and agreed to the published version of the manuscript.

Funding: The authors thank the funding support provided to this research from the National Natural Science Foundation of China (Grant No.52375517), the Key Projects of the National Natural Science Foundation of China (Grant No. 92067205), and the Aeronautical Science Foundation of China (Grant No. 2018ZE53050).

Data Availability Statement: The original contributions presented in the study are included in the article, further inquiries can be directed to the corresponding author.

Conflicts of Interest: Author Yonggang Chen was employed by the company Xi'an Aircraft Industry Group Company, Ltd. The remaining authors declare that the research was conducted in the absence of any commercial or financial relationships that could be construed as a potential conflict of interest.

References

1. Zhang, M.H.; Cao, Z.Q.; Zheng, G.; Zuo, D.Q.; Guo, C.X.; Wang, Y.H.X. Quasi-static tensile failure mechanism analysis of CFRP/Al countersunk electromagnetic riveted joints with different rivet-hole clearances. *Eng. Fail. Anal.* **2024**, *155*, 107759. [CrossRef]
2. Li, M.; Tian, W.; Hu, J.S.; Wang, C.R.; Shi, Z.H.; Liao, W.H. Influence of riveting die configuration and squeeze force on the mechanical properties and fatigue behavior of aircraft lap joints. *Eng. Fail. Anal.* **2022**, *142*, 10677. [CrossRef]
3. Zhang, Y.; Lei, B.; Wang, T.; Zhu, L.W.; Lu, Y.; Jiang, J.C. Fatigue failure mechanism and estimation of aluminum alloy self-piercing riveting at different load levels. *Eng. Fract. Mech.* **2023**, *291*, 109583. [CrossRef]
4. Skorupa, A.; Skorupa, M.; Machniewicz, T.; Korbel, A. Fatigue crack location and fatigue life for riveted lap joints in aircraft fuselage. *Int. J. Fatigue* **2014**, *58*, 209–217. [CrossRef]
5. Lv, G.C.; Li, C.Y.; Zhao, C.Y.; Jia, D.W.; Zhang, X.L.; Zhang, H.Z.; Huang, W.C. Research on theoretical prediction method of rivet-forming quality considering different riveted structure parameters. *Int. J. Adv. Manuf. Technol.* **2024**, *132*, 2333–2345. [CrossRef]
6. Jia, D.L.; Zhang, Q.H.; Xiong, L.B.; Li, J.; Bu, Y.Z.; Bao, Y. A unified evaluation method for fatigue resistance of riveted joints based on structural stress approach. *Int. J. Fatigue* **2022**, *160*, 106871. [CrossRef]
7. Di Cicco, F.; Fanelli, P.; Vivio, F. Fatigue reliability evaluation of riveted lap joints using a new rivet element and DFR. *Int. J. Fatigue* **2017**, *101*, 430–438. [CrossRef]
8. Liang, Q.X.; Zhang, T.P.; Zhu, C.R.; Bi, Y.B. Effect of riveting angle and direction on fatigue performance of riveted lap joints. *Coatings* **2021**, *11*, 236. [CrossRef]
9. Nejad, R.M.; Berto, F.; Tohidi, M. Fatigue performance prediction of Al-alloy 2024 plates in riveted joint structure. *Eng. Fail. Anal.* **2021**, *126*, 105439. [CrossRef]
10. Zhang, K.F.; Cheng, H.; Li, Y. Riveting process modeling and simulating for deformation analysis of aircraft's thin-walled sheet-metal parts. *Chin. J. Aeronaut.* **2011**, *24*, 369–377. [CrossRef]
11. Chang, Z.P.; Wang, Z.Q.; Xie, L.L.; Kang, Y.G.; Xu, M.H.; Wang, Z.M. Prediction of riveting deformation for thin-walled structures using local-global finite element approach. *Int. J. Adv. Manuf. Technol.* **2018**, *97*, 2529–2544. [CrossRef]

12. Liu, G.; Huan, H.L.; Ke, Y.L. Study on analysis and prediction of riveting assembly variation of aircraft fuselage panel. *Int. J. Adv. Manuf. Technol.* **2014**, *75*, 991–1003. [CrossRef]
13. Wang, H. Riveting sequence study of horizontal stabilizer assembly using finite-element analysis and riveting equivalent unit. *J. Aerosp. Eng.* **2014**, *27*, 04014040. [CrossRef]
14. Kondo, A.; Kasahara, T.; Kanda, A. A simplified finite element model of riveted joints for structural analyses with consideration of nonlinear load-transfer characteristics. *Aerospace* **2021**, *8*, 196. [CrossRef]
15. Ni, J.; Tang, W.C.; Xing, Y.; Ben, K.C.; Li, M. A Local-to-Global Dimensional Error Calculation Framework for the Riveted Assembly Using Finite-Element Analysis. *J. Manuf. Sci. Eng.* **2016**, *138*, 031004. [CrossRef]
16. Siahaan, R. Structural Behaviour and Design of Rivet Fastened Rectangular Hollow Flange Channel Beams. Ph.D. Thesis, Queensland University of Technology, Brisbane City, Australia, 2017.
17. Yin, J.Q.; Gu, J.Y.; Chen, Y.D.; Zhang, F. Global sensitivity analysis of riveting parameters based on a random sampling-high dimensional model representation. *Int. J. Adv. Manuf. Technol.* **2021**, *113*, 465–472. [CrossRef]
18. Wang, Z.Q.; Chang, Z.P.; Luo, Q.; Hua, S.G.; Zhao, H.T.; Kang, Y.G. Optimization of riveting parameters using Kriging and particle swarm optimization to improve deformation homogeneity in aircraft assembly. *Adv. Mech. Eng.* **2017**, *9*, 1687814017719003. [CrossRef]
19. Yang, D.; Qu, W.-W.; Ke, Y.-L. Evaluation of residual clearance after pre-joining and pre-joining scheme optimization in aircraft panel assembly. *Assem. Autom.* **2016**, *36*, 376–387. [CrossRef]
20. Xu, W.-C.; Wang, D.-F. Fatigue and impact analysis and multi-objective optimization design of Mg/Al assembled wheel considering riveting residual stress. *Front. Mech. Eng.* **2022**, *17*, 45. [CrossRef]
21. Han, Z.-P.; Wang, Y.; Tian, D. Ant colony optimization for assembly sequence planning based on parameters optimization. *Front. Mech. Eng.* **2021**, *16*, 393–409. [CrossRef]
22. Chen, B.J.; Xiao, Z.M.; Liew, K.M. A line dislocation interacting with a semi-infinite crack in piezoelectric solid. *Int. J. Eng. Sci.* **2004**, *42*, 1–11. [CrossRef]
23. Daoud, M.; Chatelain, J.F.; Bouzid, A. Effect of rake angle-based Johnson-Cook material constants on the prediction of residual stresses and temperatures induced in Al2024-T3 machining. *Int. J. Mech. Sci.* **2017**, *122*, 392–404. [CrossRef]
24. Yin, J.Q.; Wang, Z.Q.; Kang, Y.G.; Hu, Y.L. Research on the maximum riveting force based on theory of compression instability. *Adv. Mater. Res.* **2013**, *716*, 744–748. [CrossRef]
25. Chang, Z.Q.; Wang, Z.Q.; Jiang, B.; Zhang, J.M.; Guo, F.Y.; Kang, Y.G. Modeling and predicting of aeronautical thin-walled sheet metal parts riveting deformation. *Assem. Autom.* **2016**, *36*, 296–307. [CrossRef]

Disclaimer/Publisher's Note: The statements, opinions and data contained in all publications are solely those of the individual author(s) and contributor(s) and not of MDPI and/or the editor(s). MDPI and/or the editor(s) disclaim responsibility for any injury to people or property resulting from any ideas, methods, instructions or products referred to in the content.